

CountZES: Counting via Zero-Shot Exemplar Selection

Muhammad Ibraheem Siddiqui¹ Muhammad Haris Khan¹

Abstract

Object counting in complex scenes is particularly challenging in the zero-shot (ZS) setting, where instances of unseen categories are counted using only a class name. Existing ZS counting methods that infer exemplars from text often rely on off-the-shelf open-vocabulary detectors (OVDs), which in dense scenes suffer from semantic noise, appearance variability, and frequent multi-instance proposals. Alternatively, random image-patch sampling is employed, which fails to accurately delineate object instances. To address these issues, we propose CountZES, an inference-only approach for object counting via ZS exemplar selection. CountZES discovers diverse exemplars through three synergistic stages: Detection-Anchored Exemplar (DAE), Density-Guided Exemplar (DGE), and Feature-Consensus Exemplar (FCE). DAE refines OVD detections to isolate precise single-instance exemplars. DGE introduces a density-driven, self-supervised paradigm to identify statistically consistent and semantically compact exemplars, while FCE reinforces visual coherence through feature-space clustering. Together, these stages yield a complementary exemplar set that balances textual grounding, count consistency, and feature representativeness. Experiments on diverse datasets demonstrate CountZES superior performance among ZOC methods while generalizing effectively across domains. Code is available at [GitHub](#).

1. Introduction

Object counting plays a vital role in a wide range of applications. Traditional counting approaches are typically *class-specific*, tailored for predefined categories such as crowds (Babu Sam et al., 2022), vehicles (Li et al., 2020), or cells (Tyagi et al., 2023). However, these methods require

¹Mohamed Bin Zayed University of Artificial Intelligence. Correspondence to: Muhammad Ibraheem Siddiqui <muhammad.siddiqui@mbzauai.ac.ae>.

Preprint. February 4, 2026.

Performance across Natural, Aerial and Medical Domains

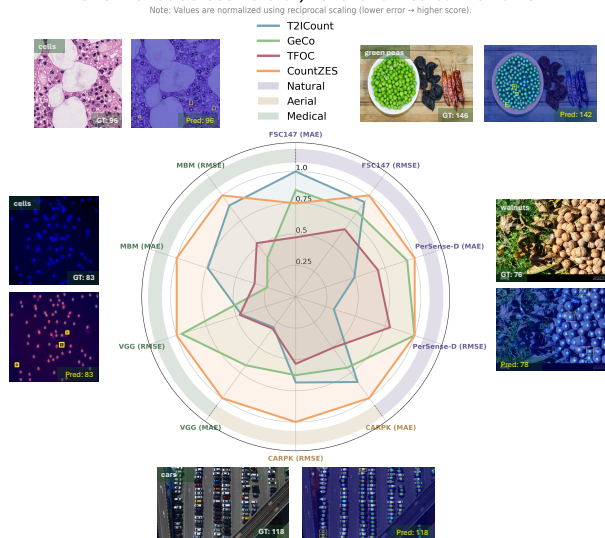


Figure 1. Zero-shot object counting comparison of our CountZES against T2ICount (Qian et al., 2025), GeCo (Pelhan et al., 2024a), and TFOC (Shi et al., 2024) across diverse benchmarks spanning natural, aerial, and medical domains.

retraining whenever a new class is introduced, limiting their scalability. To overcome this, *class-agnostic counting* has emerged, aiming to generalize to unseen categories (Yang et al., 2021; Huang et al., 2023; Hui et al., 2024). Existing class-agnostic methods can be categorized into three paradigms: *few-shot object counting* (FSOC), *reference-less counting* (RLC), and *zero-shot object counting* (ZOC).

FSOC methods rely on a small set of annotated exemplars provided at inference, which limits scalability (Zhai et al., 2024; Zhang et al., 2025). In contrast, RLC estimates counts directly from global visual cues (Hobley & Prisacariu, 2023; D’Alessandro et al., 2024), but lacks semantic awareness and tends to focus on visually dominant patterns (Xu et al., 2023; Zhu et al., 2024). To address these issues, ZOC has emerged as a promising direction (Jiang et al., 2023; Xu et al., 2023; Kang et al., 2024), enabling the counting of arbitrary unseen categories from text prompts alone.

Current ZOC methods fall into three main streams. (1) Image–text interaction–based methods leverage vision–language models (VLMs) to align text and image embeddings for density regression. While scalable to unseen

classes, they often fail to capture fine-grained visual details, especially for atypical objects (Jiang et al., 2023). (2) Class-relevant exemplar selection discover visual patches that align with the target class by comparing arbitrarily sampled regions with class prototypes (Xu et al., 2023), but random sampling often produces partial or noisy exemplars. (3) To overcome this, detection-driven exemplar selection employs open-vocabulary detectors (OVD) to propose text-conditioned boxes as candidate exemplars. However, OVDs often fail to provide clean single-instance exemplars, especially in dense scenes. For example, VA-Count (Zhu et al., 2024) employs GroundingDINO (Liu et al., 2024) to extract candidate exemplars and then uses a binary filter to verify single-object instances. However, this pipeline struggles when GroundingDINO provides few or no single-instance boxes, Figure. 2(a). Furthermore, counting accuracy is sensitive to exemplar choice and randomly selected exemplars are often insufficiently representative of the target instances, leading to underestimated object counts, Figure. 2(b).

Despite its importance, exemplar selection in ZOC remains largely underexplored. Existing methods, such as ZSOC (Xu et al., 2023) and VA-Count, rely on random patch sampling or simple confidence-based filtering of OVD detections, respectively. However, object counting is inherently a dense prediction task that poses challenges fundamentally different from those in sparse settings. Heavy occlusion, scale variation, and tightly packed instances make patch-level sampling or off-the-shelf detection unreliable, Figure. 2(a). A natural alternative would be to train dedicated dense detectors like GeCo (Pelhan et al., 2024a). However, such approaches require costly box-level annotations in dense scenes and often internalize dataset-specific priors, resulting in limited cross-domain generalization (see GeCo in Figure. 1). Moreover, retraining or finetuning off-the-shelf vision backbones for each new domain not only requires large-scale annotated training data but is computationally expensive and impractical in real-world settings. This motivates the need for approaches that can fully exploit the rich representations of pretrained foundation models like CLIP (Radford et al., 2021) and SAM (Kirillov et al., 2023) while avoiding task-specific supervision. Existing inference-only approaches, such as TFOC (Shi et al., 2024) and TFCAC (Lin et al., 2025), primarily treat the ZOC task as a segmentation problem, relying solely on SAM, which exhibits limited performance in dense and congested scenes (Ma et al., 2023). Although exemplar-based density estimation has long been recognized as highly effective for dense counting scenarios (Liu et al., 2018), to our knowledge, no existing inference-only approach targets exemplar selection in ZOC.

To fill this gap, we introduce CountZES, an inference-only pipeline for object counting via zero-shot exemplar selection, Figure. 2(c). CountZES formulates exemplar discovery

as a multi-stage process comprising Detection-Anchored Exemplar (DAE), Density-Guided Exemplar (DGE), and Feature-Consensus Exemplar (FCE) stages. Each stage contributes an exemplar, resulting in a complementary set that balances textual alignment, count-driven consistency, and feature-level representativeness, respectively. We thus cast zero-shot counting as an exemplar inference problem under semantic, statistical, and feature-level priors. Importantly, CountZES adopts an inference-only exemplar selection pipeline that operates without any ZOC-specific finetuning. While the framework leverages pretrained VLM, segmentation, and density-estimation components for semantic alignment and counting, these models remain fixed and are not optimized within CountZES. This design enables improved generalization, which is validated through extensive evaluations across diverse benchmarks spanning natural, aerial, and medical domains (Figure. 1). In summary, we make following core contributions:

- We propose CountZES, an inference-only pipeline for ZOC via principled exemplar selection across three stages (DAE, DGE, and FCE) that collectively balance textual grounding, count consistency, and feature representativeness, yielding a diverse exemplar set.
- CountZES introduces dedicated modules at each stage: *Similarity-guided SAM-based Exemplar Selection (SSES)* refines coarse multi-instance OVD detections into precise single-instance exemplars; *Peak-to-Point (P2P) prompting with RoI count-based filtering* enables density-driven exemplar discovery; and *Pseudo-GT Guided Exemplar Selection (GGES)* together with *Feature-based Representative Exemplar Selection (FRES)* refines exemplars via statistical consistency and feature-level consensus.
- Being an inference-only exemplar selection approach, CountZES avoids ZOC-specific optimization and demonstrates strong generalization across datasets and domains. Extensive experiments on natural, aerial, and medical counting benchmarks validate its robustness and superior performance compared to SOTA methods.

2. Related Work

To eliminate the dependence on manually annotated exemplars in FSOC methods (Lu et al., 2018; Ranjan et al., 2021; Liu et al., 2022; DJukic et al., 2023; He et al., 2024), Xu et al. (Xu et al., 2023) introduce the ZOC task, which estimates object counts from a class name by employing a text-conditioned variational autoencoder (VAE) that synthesizes visual exemplars through patch-prototype pseudo-labels. However, the arbitrary selection of patches hinders precise object delineation, thereby degrading exemplar quality. Subsequent works (Jiang et al., 2023; Kang et al., 2024; Amini

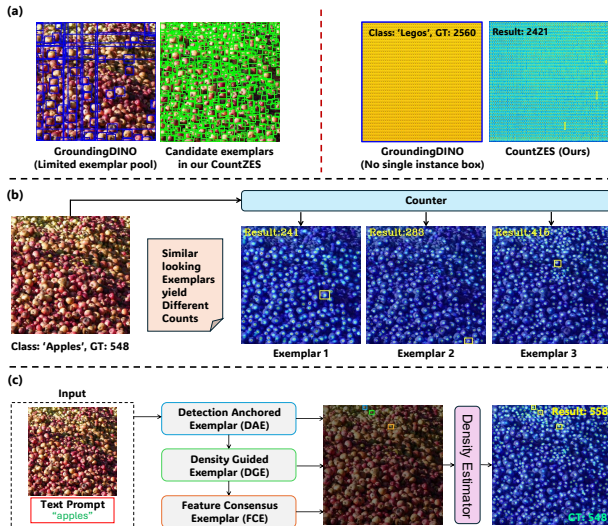


Figure 2. (a) Detectors like GroundingDINO (Liu et al., 2024) often yield very few or even fail to provide single instance boxes. (b) Counting is sensitive to exemplar choice. (c) Introducing CountZES a multi-stage inference-only exemplar selection approach for ZOC. (Best viewed in zoom).

et al., 2023) leverage image–text alignment to model object–class correlations without relying on visual exemplars, enhancing scalability but often failing to preserve structural detail for irregularly shaped objects. Detection-driven approaches such as DAVE (Pelhan et al., 2024b) adopt a detect-and-verify pipeline but bias toward majority-class counts (Qian et al., 2025). Recent VLM-based frameworks like PseCo (Huang et al., 2024) employs a three-stage point, segment and count design integrating SAM (Kirillov et al., 2023) for segmentation and CLIP (Radford et al., 2021) for verification, while GeCo (Pelhan et al., 2024a) unifies detection, segmentation, and counting with a single-stage dense query encoder–decoder architecture. VA-Count (Zhu et al., 2024) instead leverages GroundingDINO for text-guided detection and performs a simple logits-based exemplar selection, yielding limited exemplar diversity and relying on DINO’s initial proposals (often multi-instance boxes). Our CountZES explicitly handles the challenge of limited or no single instance boxes coming from the detector and multi-stage exemplar selection under semantic, statistical, and feature-level priors results in diverse exemplars. Finally, T2ICount (Qian et al., 2025) exploits text-to-image diffusion priors for open-world counting but exhibits limited cross-domain generalization due to dataset-specific ZOC optimization (Figure. 1). In contrast, our CountZES being inference-only demonstrates superior generalization. Among the inference-only approaches TFOC (Shi et al., 2024), TFCAC (Lin et al., 2025), and OmniCount (Mondal et al., 2025) formulate counting as a segmentation problem and are constrained by the limited performance of SAM in handling small and congested objects (Ma et al., 2023).

3. Method

Zero-shot exemplar discovery in dense scenes is inherently ambiguous due to semantic noise, multi-instance proposals, and appearance variability. To address these challenges, we introduce CountZES, an inference-only framework for ZOC (Figure. 3), which discovers a diverse exemplar set through three synergistic stages, namely DAE (Sec. 3.1), DGE (Sec. 3.2), and FCE (Sec. 3.3). DAE performs semantic grounding and single-instance isolation, DGE enforces statistical reliability via density-based self-supervision and pseudo-GT consistency, and FCE promotes visual representativeness through feature-level consensus.

3.1. Detection Anchored Exemplar (DAE)

Given an image $I \in \mathbb{R}^{H \times W \times 3}$ and a text prompt t (Fig. 3), we compute CLIP similarity $S \in [0, 1]^{H \times W}$ to highlight regions semantically aligned with t , while GroundingDINO simultaneously generates text-aligned object proposals.

Initial Box Selection: Each detection box \mathbf{b}_i serves as a candidate region, within which S provides fine-grained confidence cues about semantic alignment with t . However, not all detections correspond to clean, single-instance regions, as some may encompass multiple instances or include background areas. To quantify the internal consistency of each region, we require a measure that captures how concentrated or dispersed the similarity responses are within the box. We therefore compute the *entropy* of the CLIP similarity distribution inside \mathbf{b}_i , which reflects the spatial uniformity of similarity values (see Appendix. A.3 for details). Intuitively, boxes that include multiple objects or background exhibit high entropy due to fluctuating similarity responses across diverse semantic areas. In contrast, a box that tightly encloses a single, well-aligned instance yields low entropy, indicating coherent similarity responses in S .

Let c_i denote the confidence of the i^{th} detection from GroundingDINO, and $\hat{H}(\mathbf{b}_i)$ the normalized entropy of similarity values within its bounding box \mathbf{b}_i . Each box is assigned a composite score balancing detection confidence and the inverse entropy term:

$$J_{\text{box}}(\mathbf{b}_i) = \alpha c_i + (1 - \alpha) (1 - \hat{H}(\mathbf{b}_i)), \quad (1)$$

where $\alpha = 0.5$ controls the trade-off between *semantic confidence* and *spatial purity*, the latter reflecting how consistent S is within \mathbf{b}_i . Higher $J_{\text{box}}(\mathbf{b}_i)$ indicates boxes that are both confident (high c_i) and internally consistent (low \hat{H}), favoring single-instance regions over cluttered ones. The top-scoring box, $\mathbf{b}^c = \arg \max_{\mathbf{b}_i} J_{\text{box}}(\mathbf{b}_i)$, is selected as the *coarse region of interest*. Why coarse? Although this entropy-weighted scoring favors regions with fewer overlapping instances or backgrounds, it does not guarantee that the selected box strictly contains a single instance. When all GroundingDINO detections correspond to grouped regions,

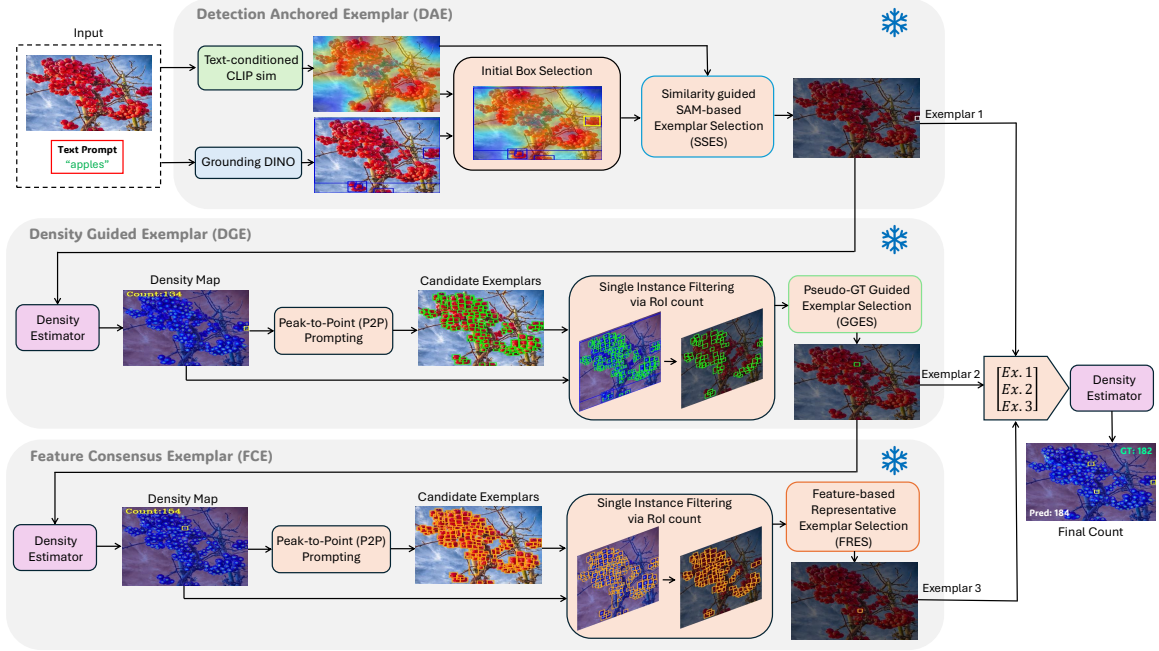


Figure 3. Overview of CountZES. The pipeline operates in three stages. DAE refines GroundingDINO detections using CLIP similarity via SSES to obtain text-aligned single-instance regions. DGE then adopts a density-driven paradigm: it generates a density map conditioned on DAE exemplar, leverages P2P prompting to identify candidate exemplars, applies RoI-based single-instance filtering, and selects the most reliable exemplar through GGES. Finally, FCE focuses on visual coherence by projecting candidate exemplars onto SAM’s feature map and using FRES to select the representative exemplar. An exemplar from each stage form a diverse exemplar set for final object count.

even the top-scoring box may include multiple instances. Hence, this coarse selection is refined next by the SSES module to obtain an instance-specific region.

Sim-guided SAM-based Exemplar Selection (SSES): Given the coarse region \mathbf{b}^c , SSES refines it into a clean, instance-specific exemplar by leveraging the similarity map S and SAM’s segmentation capability (see Figure. 9). The core intuition is that regions containing well-aligned object instances will exhibit distinct peaks in S , representing local maxima of semantic alignment with the target text. To identify high-similarity regions, we sample k peaks from S within \mathbf{b}^c by applying percentile-based threshold rather than a fixed similarity cutoff. Percentiles are computed over the full similarity map S , normalizing thresholds to each image’s global similarity statistics. Starting from a high percentile (e.g., 90th), the threshold is gradually relaxed in fixed steps ($\Delta p = 10$) until at most $k = 16$ peaks are detected within \mathbf{b}^c (see Appendix A.1). This adaptive relaxation dynamically adjusts the confidence level for peak selection based on the strength and density of responses in the coarse region. Formally, for a percentile p , the threshold is defined as $\tau(p) = \text{Perc}_p(S)$, and we retain spatial locations inside $\Omega(\mathbf{b}^c) = \{(x, y) \mid x_0 \leq x \leq x_1, y_0 \leq y \leq y_1\}$ whose similarity values exceed this threshold:

$$\mathcal{Q}(p) = \{q = (x, y) \in \Omega(\mathbf{b}^c) \mid S(q) \geq \tau(p)\}, \quad (2)$$

where q denotes a local peak in S , and $\mathcal{Q}(p)$ represents the

set of spatial locations within \mathbf{b}^c whose similarity values surpass the global percentile threshold $\tau(p)$. This percentile-based strategy identifies strong responses across regions, while the relaxation mechanism enables the selection of high-confidence peaks even under low-contrast similarity distributions. Each selected peak q_i is then passed as a positive point prompt to SAM, generating a binary mask $M_i = \mathcal{P}(I; q_i)$. For each mask, we compute two complementary measures: (1) *semantic strength* $\text{Sim}(M_i)$, which quantifies how strongly the pixels within M_i align with the text prompt t via the mean percentile rank of their similarity values in S , i.e., $\text{Sim}(M_i) = \frac{1}{|M_i|} \sum_{u \in M_i} r(u)$, where $r(u)$ is the percentile rank of $S(u)$; and (2) *normalized entropy* $\hat{H}(M_i)$, which captures how uniformly these similarity values are distributed. While $\text{Sim}(M_i)$ favors semantically aligned regions, $\hat{H}(M_i)$ penalizes masks with diffuse or multi-object content. Each mask is then assigned a composite score that balances the two measures:

$$J_{\text{mask}}(M_i) = w_{\text{sim}} \text{Sim}(M_i) + w_{\text{ent}} (1 - \hat{H}(M_i)), \quad (3)$$

where $w_{\text{sim}} = w_{\text{ent}} = 0.5$. The optimal mask is selected as $M_{\text{DAE}} = \arg \max_{M_i} J_{\text{mask}}(M_i)$, and its corresponding bounding box (\mathbf{b}_{DAE}) defines the refined, instance-specific region. In essence, SSES acts as a fine-grained refinement stage, transforming the coarse detector-derived region \mathbf{b}^c into a single-instance exemplar \mathbf{b}_{DAE} .

3.2. Density-Guided Exemplar (DGE)

Peak-to-Point (P2P) prompting: Given the input image I and exemplar \mathbf{b}_{DAE} , the density estimator produces a density map $D \in \mathbb{R}^{H \times W}$, where each pixel value estimates the expected object count (Figure. 3). The total count is $C = \sum_{x,y} D(x,y)$, and prominent local maxima in D correspond to potential object centers. Rather than assuming a specific distribution for D , we employ the mean and standard deviation of the density map as adaptive scale statistics to identify high-confidence peaks. Specifically, an adaptive threshold is defined as $T_D = \mu_D + 2\sigma_D$, where μ_D and σ_D denote the mean and standard deviation of D , respectively. This criterion highlights salient density responses while suppressing background noise, even when the underlying distribution is skewed. Pixels satisfying $D(x,y) \geq T_D$ are retained as high-confidence candidates. Distinct peaks are then extracted via local peak detection within a fixed neighborhood to ensure spatial separation:

$$\mathcal{P} = \{p_i = (x_i, y_i) \mid D(p_i) \geq T_D\}. \quad (4)$$

To ensure semantic consistency with GroundingDINO detections, we apply box gating, retaining only peaks p_i that fall within at least one detection box $\mathbf{b}_j^{\text{DINO}}$. The filtered prompt set is thus $\mathcal{P}^* = \{p_i \in \mathcal{P} \mid p_i \in \Omega_{\text{DINO}}\}$, where Ω_{DINO} denotes the union of all detection boxes. Each surviving point $p_i \in \mathcal{P}^*$ is used as a positive prompt for SAM, generating a binary mask $M_i = \mathcal{P}(I; p_i)$ and its corresponding bounding box \mathbf{b}_i . These boxes then serve as candidate exemplars for subsequent selection (see Appendix. A.2).

Single-instance filtering via RoI count: To verify whether \mathbf{b}_i captures a single instance, we compute its integrated density within the region of interest (RoI):

$$\hat{c}(\mathbf{b}_i) = \sum_{(x,y) \in \Omega(\mathbf{b}_i)} D(x,y), \quad (5)$$

where $\Omega(\mathbf{b}_i)$ denotes the set of pixel coordinates inside the box. This operation is conceptually inspired by the *RoI pooling* mechanism in Fast R-CNN (Girshick, 2015). Since regression noise and density diffusion may yield fractional counts above one, boxes with predicted counts satisfying $1 < \hat{c}(\mathbf{b}_i) < 2$ are retained as single-instance candidates. The resulting subset $\mathcal{B}_{\text{single}}$ represents single-instance proposals for subsequent exemplar refinement (see Figure. 10).

Pseudo-GT guided exemplar selection (GGES): To identify the most reliable exemplar within $\mathcal{B}_{\text{single}}$, we estimate a pseudo-GT count via consensus among all single-instance candidates. Rather than relying on discrete per-box predictions $\hat{c}_i = \hat{c}(\mathbf{b}_i)$, we model their empirical distribution using a non-parametric probability density function (PDF), (see Appendix. A.3). This PDF reveals the dominant count region, consolidating multiple uncertain predictions into

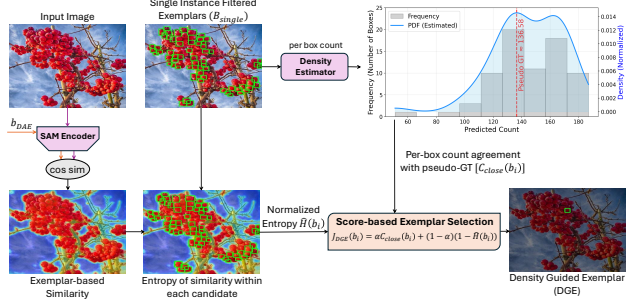


Figure 4. Overview of GGES in the DGE stage. Per-box counts from single-instance candidates are used to estimate a pseudo-GT count via density estimator. A SAM-based similarity map, conditioned on \mathbf{b}_{DAE} , captures semantic correspondence, and a composite score based on count proximity to the pseudo-GT and similarity-map entropy guides density-guided exemplar selection.

a stable pseudo-GT reference (Figure. 4). By leveraging the overall distribution instead of individual estimates, this approach mitigates outlier effects and guides exemplar selection toward the statistically most consistent estimate.

Each candidate box \mathbf{b}_i is then evaluated for its predicted count closeness to the pseudo-GT count, defined as $C_{\text{close}}(\mathbf{b}_i)$. Higher $C_{\text{close}}(\mathbf{b}_i)$ indicate higher representativeness as a density-guided single-instance exemplar. However, count consistency alone does not ensure semantic purity. A region may agree with pseudo-GT yet still include clutter or background. To assess the semantic compactness of each candidate region, we compute an exemplar-conditioned SAM similarity map. Unlike the DAE stage, where a text-conditioned CLIP similarity map was used due to the absence of a concrete exemplar, the DGE stage benefits from having the previously obtained \mathbf{b}_{DAE} exemplar. This enables a more discriminative and instance-specific similarity computation. Specifically, \mathbf{b}_{DAE} is passed through SAM’s encoder to obtain its feature embedding, which is then compared, via cosine similarity, with the spatial embeddings of the entire image. The resulting similarity map provides a more discriminative and instance-specific representation, highlighting regions that share strong visual and structural correspondence with the exemplar (Figure. 4).

The normalized entropy of this similarity map within each box \mathbf{b}_i , denoted as $\hat{H}(\mathbf{b}_i)$, quantifies how spatially concentrated the exemplar’s feature activation is. Low entropy indicates compact, object-specific responses, while high entropy suggests background interference or multiple objects. Thus, $\hat{H}(\mathbf{b}_i)$ complements $C_{\text{close}}(\mathbf{b}_i)$ by ensuring the exemplar is both statistically consistent and semantically pure. Each candidate is scored as follows:

$$J_{\text{DGE}}(\mathbf{b}_i) = \alpha C_{\text{close}}(\mathbf{b}_i) + (1 - \alpha)(1 - \hat{H}(\mathbf{b}_i)), \quad (6)$$

where $\alpha = 0.5$ balances count consistency and semantic compactness. The box with highest score is selected as DGE, given as $\mathbf{b}_{\text{DGE}} = \arg \max_{\mathbf{b}_i \in \mathcal{B}_{\text{single}}} J_{\text{DGE}}(\mathbf{b}_i)$. DGE

thus complements DAE by introducing a count-driven self-supervised perspective. By grounding exemplar selection in the predicted density rather than textual cues, DGE enhances coverage and robustness, particularly in cluttered scenes where text-conditioned grounding alone is insufficient.

3.3. Feature-Consensus Exemplar (FCE)

While DGE enforces statistical consistency via pseudo-GT estimation, it does not explicitly capture visual coherence among candidate instances. The FCE stage refines exemplar selection at the feature level, ensuring visual representativeness of the dominant object appearance within the scene. Unlike DAE, which begins from text-conditioned grounding, FCE builds upon the exemplar from the DGE stage, \mathbf{b}_{DGE} . Using \mathbf{b}_{DGE} as the anchor, FCE regenerates a density map, and performs P2P prompting followed by single-instance filtering, mirroring the steps of DGE up to the formation of $\mathcal{B}_{\text{single}}$. However, instead of pseudo-GT guided selection, FCE introduces FRES module discussed next.

Feature-based Rep Exemplar Selection (FRES): Given $\mathcal{B}_{\text{single}}$, our goal is to identify the exemplar that most effectively captures the dominant visual appearance of the object class (Fig. 5). The image I is first passed through SAM’s encoder to obtain a dense feature map $\Phi \in \mathbb{R}^{256 \times 64 \times 64}$. Since projecting small boxes onto this low-resolution map may cause spatial detail loss, Φ is upsampled to $\Phi^{\text{up}} \in \mathbb{R}^{256 \times 256 \times 256}$ using window attention-based upsampling as in (Wimmer et al., 2025). Each candidate box \mathbf{b}_i is then projected onto Φ^{up} , and the corresponding region $\Phi^{\text{up}}(\Omega_f(\mathbf{b}_i))$ defines its local feature subset. Finally, each box descriptor \mathbf{v}_i is computed via spatial average pooling:

$$\mathbf{v}_i = \frac{1}{|\Omega_f(\mathbf{b}_i)|} \sum_{(u,v) \in \Omega_f(\mathbf{b}_i)} \Phi^{\text{up}}(:, v, u), \quad (7)$$

The vector \mathbf{v}_i thus represents the semantic appearance of region \mathbf{b}_i in the SAM feature space. Since the magnitude of pooled features may vary with object size, texture, or illumination, direct comparison between descriptors can be biased toward high-energy regions. To mitigate this effect, we apply ℓ_2 -normalization so that all descriptors lie on a unit hypersphere, ensuring that their pairwise dot products correspond to cosine similarity.

While each descriptor \mathbf{v}_i captures the visual characteristics of a single-instance region, these descriptors may still vary due to pose, scale, illumination, or minor background interference. To isolate the most representative exemplar, we cluster the descriptors in feature space to identify the dominant appearance pattern. Specifically, we cluster \mathbf{v}_i into two groups using cosine similarity, forming a majority and a minority cluster. This partition effectively separates the visually consistent, frequently occurring appearances from peripheral or noisy ones. The majority cluster \mathcal{C}_{maj} captures

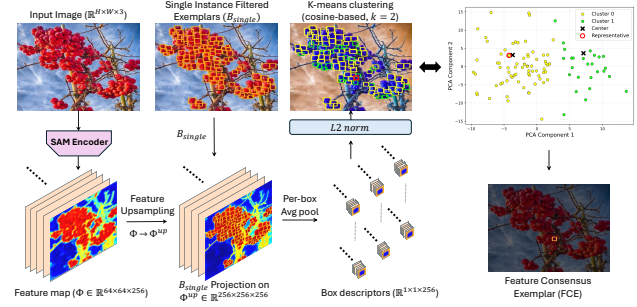


Figure 5. Overview of FRES module in the FCE stage. Single-instance boxes $\mathcal{B}_{\text{single}}$ are projected onto SAM’s upsampled feature map Φ^{up} to obtain ℓ_2 -normalized regional embeddings. These embeddings are clustered, and the box closest to the majority-cluster centroid is selected as the representative exemplar.

the dominant object appearance, and the exemplar whose descriptor is closest to its centroid is selected as the representative exemplar, $\mathbf{b}_{\text{FCE}} = \arg \max_{\mathbf{b}_i \in \mathcal{C}_{\text{maj}}} s(\mathbf{v}_i, \mu_{\text{maj}})$. Where $s(\cdot, \cdot)$ denotes cosine similarity and μ_{maj} is the mean feature descriptor of the majority cluster. The selected exemplar \mathbf{b}_{FCE} thus reflects the shared visual characteristics across all single-instance proposals. By grounding exemplar selection in feature-level consensus rather than count statistics, FCE complements DGE by emphasizing visual coherence.

Ultimately, \mathbf{b}_{DAE} , \mathbf{b}_{DGE} , and \mathbf{b}_{FCE} constitute the final exemplar set, which is jointly provided as multiple support exemplars to the density estimator to produce the final density map and count prediction. Selecting one exemplar per stage, rather than all exemplars from a single stage, introduces cross-perspective diversity (see ablations in Sec. 4).

4. Experiments

Datasets and Evaluation Metrics. We evaluate our CountZES on diverse benchmarks including FSC-147 (Shi et al., 2022), CARPK (Hsieh et al., 2017), PerSense-D (Siddiqui et al., 2025), and two medical cell-counting datasets, VGG (Lempitsky & Zisserman, 2010) and MBM (Paul Cohen et al., 2017). See Appendix. A.4 for dataset details. Following prior ZOC works, we employ mean absolute error (MAE) to measure counting accuracy and root mean square error (RMSE) to assess model robustness.

Implementation Details. CountZES employs CLIP (Radford et al., 2021) for text-image alignment and GroundingDINO (Liu et al., 2024) for initial box proposals, with the detection threshold set to 0.15. SAM (Kirillov et al., 2023) is used for mask generation leveraging point prompts across the SSES, GGES, and FRES modules. To demonstrate the model-agnostic nature of CountZES, we utilize CounTR (Liu et al., 2022) and DSALVANet (He et al., 2024) as pretrained off-the-shelf density estimators (DE). We distinguish between *in-domain* and *cross-domain* settings: in-domain uses a DE pretrained on the same dataset as eval-

Table 1. Comparison of CountZES with SOTA ZOC methods on FSC-147 dataset. Best results are in bold and second-best are underlined. † indicates ZOC methods based on exemplar discovery. * indicates that CountingDINO is not zero-shot (box prompts).

Method	Venue	Inference only	MAE	RMSE
ZSOC† (Xu et al., 2023)	CVPR’23	✗	22.09	115.17
CLIP-Count (Jiang et al., 2023)	ACM’23	✗	17.78	106.62
CounTX (Amini et al., 2023)	BMVC’23	✗	15.88	106.29
VLCounter (Kang et al., 2024)	AAAI’24	✗	17.05	106.16
PseCo (Huang et al., 2024)	CVPR’24	✗	16.58	129.77
DAVE (Pelhan et al., 2024b)	ICCV’24	✗	14.90	103.42
VA-Count† (Zhu et al., 2024)	ECCV’24	✗	17.88	129.31
CountGD (Amini et al., 2024)	NeurIPS’24	✗	14.76	120.42
GeCo (Pelhan et al., 2024a)	NeurIPS’24	✗	13.30	108.72
T2ICount (Qian et al., 2025)	CVPR’25	✗	<u>11.76</u>	<u>97.86</u>
CountZES† (in-domain)	(Ours)	✓	15.77	91.40
CountingDINO* (Pacini et al., 2026)	WACV’26	✓	20.93	71.37
SAM (Kirillov et al., 2023)	ICCV’23	✓	42.48	137.50
Count Anything (Ma et al., 2023)	arXiv’23	✓	27.97	131.24
G-DINO (Liu et al., 2024)	ECCV’24	✓	59.23	159.28
TFOC (Shi et al., 2024)	WACV’24	✓	24.79	137.15
TFCAC (Lin et al., 2025)	WACV’25	✓	<u>23.59</u>	<u>113.60</u>
OmniCount (Mondal et al., 2025)	AAAI’25	✓	21.46	133.28
CountZES†	(Ours)	✓	21.09	110.14

Table 2. CountZES compared to SOTA on CARPK dataset.

Method	Inference-only	MAE	RMSE
CLIP-Count (Jiang et al., 2023)	✗	11.96	16.61
CounTX (Amini et al., 2023)	✗	8.13	10.87
G-DINO (Liu et al., 2024)	✗	29.72	31.60
VLCounter (Kang et al., 2024)	✗	6.46	8.68
VA-Count (Zhu et al., 2024)	✗	10.63	13.20
GeCo (Pelhan et al., 2024a)	✗	10.34	14.73
CountGD (Amini et al., 2024)	✗	3.83	5.41
T2ICount (Qian et al., 2025)	✗	8.61	13.47
TFOC (Shi et al., 2024)	✓	14.35	17.22
OmniCount (Mondal et al., 2025)	✓	13.41	16.85
CountingDINO (Pacini et al., 2026)	✓	21.26	28.20
CountZES (Ours)	✓	7.24	9.22

uation, while cross-domain employs DE pretrained on a dataset different from the one being tested.

Quantitative Results on FSC-147. We evaluate CountZES under two configurations, as summarized in Table 1. In the *in-domain* setting, DSALVNet pretrained on FSC-147 is employed as the DE. Under this configuration, CountZES achieves the lowest RMSE and a competitive MAE among ZOC-optimized methods, despite being an inference-only framework. Compared to the leading exemplar selection-based approach, VA-Count (Zhu et al., 2024), CountZES reduces MAE by 11.8% and RMSE by 29.3%, demonstrating the effectiveness of our exemplar selection strategy. For comparison with inference-only approaches, we further evaluate CountZES in a cross-domain setting using DE pretrained on CARPK. Among inference-only methods, CountZES attains the lowest MAE and RMSE.

Quantitative Results on CARPK. We evaluate CountZES on CARPK under a cross-domain setting using DSALVNet pretrained on FSC-147 as the density estimator. As shown in Table 2, CountZES achieves the lowest MAE and RMSE among inference-only approaches, while remaining compet-

Table 3. CountZES compared to SOTA on PerSense-D dataset.

Method (Inf-only)	Density-based						Class-wise	
	Low		Med		High		Overall	
	MAE	RMSE	MAE	RMSE	MAE	RMSE	MAE	RMSE
GeCo (✗)	11.63	17.84	10.30	20.61	12.38	24.13	13.12	28.36
T2ICount (✗)	30.04	122.91	25.16	76.95	20.62	52.23	24.95	88.21
TFOC (✓)	7.20	10.36	16.07	21.63	36.88	63.82	17.79	35.74
CountZES (✓)	6.86	19.22	10.26	14.44	<u>20.36</u>	<u>43.65</u>	12.29	28.32

Table 4. Comparison of CountZES with SOTA ZOC methods on medical cell counting datasets VGG and MBM.

Method (Inf-only)	VGG		MBM	
	MAE	RMSE	MAE	RMSE
GeCo (✗)	<u>67.32</u>	<u>77.53</u>	92.59	104.52
T2ICount (✗)	151.35	162.81	<u>30.01</u>	44.44
TFOC (✓)	144.91	158.52	64.25	75.67
CountZES (✓)	45.55	74.41	22.16	40.06

itive with ZOC-optimized methods that rely on task-specific training. We attribute this strong generalization to the proposed multi-stage exemplar selection strategy, which selects representative single-instance exemplars by leveraging complementary semantic, statistical, and feature-level cues. This principled exemplar selection without task-specific training enables robust counting even under substantial domain shift.

Quantitative Results on PerSense-D. Following the same cross-dataset evaluation protocol, we evaluate CountZES on the PerSense-D dataset using CounTR pretrained on FSC147 (Table 3). In addition to overall category-wise performance, we conduct fine-grained analysis across three density-based splits; *low*, *medium*, and *high*, as defined in (Siddiqui et al., 2025). CountZES consistently achieves competitive performance across varying crowding conditions, outperforming the inference-only approach TFOC and remaining comparable to ZOC-optimized methods. Notably, 16 out of 28 classes ($\approx 57\%$) in PerSense-D overlap with FSC-147, but still T2ICount, which achieves strong in-domain performance on FSC-147, struggles on PerSense-D. We attribute this degradation to the reliance on textual supervision during training in T2ICount, which couples linguistic priors with numerical estimation. Such entanglement is particularly brittle under distribution shift, where object appearance, density, and scale differ substantially across datasets. In contrast, CountZES employs textual input solely as an inference-time semantic probe to guide exemplar discovery, while the counting backbone remains purely visual and exemplar-driven. By decoupling textual guidance from numerical estimation, it mitigates text-induced bias and preserves semantic flexibility, thereby improving robustness to distributional shifts for the same category across datasets.

Quantitative Results on VGG and MBM. To further assess the cross-domain generalization capability of CountZES, we evaluate it on two medical-domain cell counting

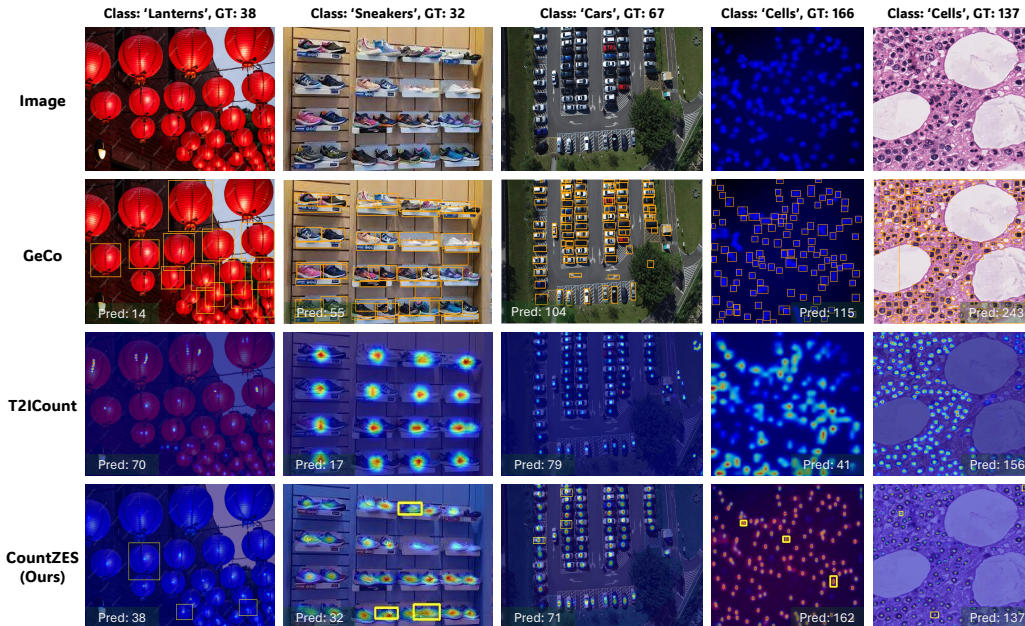


Figure 6. Qualitative comparison of CountZES with T2ICount (Qian et al., 2025) and GeCo (Pelhan et al., 2024a) across diverse scenarios, including natural (FSC-147 and PerSense-D), aerial (CARPK), and medical cell-counting (VGG and MBM) images.

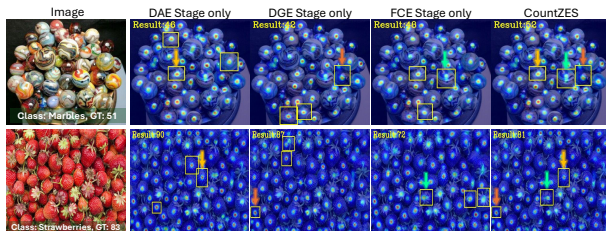


Figure 7. Demonstrates complementary nature of DAE, DGE and FCE stages. For each stage, the top three exemplars are shown with their counting outputs. One exemplar from each stage (arrows) provides complementary cues, and their combination in CountZES improves overall counting performance (last column).

datasets: VGG and MBM. As summarized in Table 4, CountZES achieves remarkable cross-domain performance, outperforming both inference-only and ZOC-optimized approaches by a substantial margin.

Qualitative Result & Runtime Efficiency. Fig. 6 presents a qualitative comparison between CountZES and SOTA methods on diverse images, spanning natural, aerial, and medical domains. On average, CountZES infers the total count in 2.3 seconds per image and achieves the best performance–runtime tradeoff among inference-only approaches (see Figure. 11 and Appendix A.6).

Ablation Study. Since each stage builds upon the exemplar generated by the previous one, we perform a progressive ablation to quantify the incremental contribution of each stage toward overall counting performance. As shown in Table 5, adding successive stages consistently improves accuracy, validating their complementary roles. Finally, to examine

Table 5. Ablation study for CountZES on FSC-147 dataset: (left) stage-wise contribution; (right) demonstrates the advantage of cross-stage collaboration over single-stage exemplar selection.

DAE	DGE	FCE	MAE	RMSE
●	○	○	25.13	97.40
○	●	○	20.75	92.36
○	○	●	15.77	91.40

Configuration	MAE	RMSE
DAE only	21.73	118.03
DGE only	17.38	108.56
FCE only	19.42	116.53
CountZES	15.77	91.40

the diversity induced by each stage in exemplar selection, we conduct another ablation under a consistent 3-exemplar setting by selecting the top three exemplars from each stage and comparing them against the standard CountZES configuration that uses one exemplar per stage (Table 5). The latter achieves superior performance (Figure. 7), indicating that cross-stage collaboration yields a richer, complementary, and more balanced exemplar set than any stage in isolation. We discuss the limitations of CountZES in Appendix. A.7.

5. Conclusion

We presented CountZES, an inference-only framework for ZOC, which formulates exemplar discovery as a three-stage process (DAE, DGE, and FCE), each contributing complementary cues from semantic, statistical, and visual perspectives. DAE ensures text-grounded semantic alignment, DGE introduces density-driven numerical consistency, and FCE enforces feature-level consensus to identify representative exemplars. This induces diversity into the exemplar set, thereby enhancing counting performance. Extensive experiments across multiple domains demonstrate its generalization and superior performance compared to SOTA.

Broader Impact: This paper presents work whose goal is to advance the field of machine learning. At present, we do not anticipate any discernible adverse ethical or social implications of our work.

References

- Amini, N., Amini-Naieni, K., Han, T., and Zisserman, A. Open-world text-specified object counting. In *BMVC*, 2023.
- Amini, N., Han, T., and Zisserman, A. Countgd: Multimodal open-world counting. *Advances in Neural Information Processing Systems*, 37:48810–48837, 2024.
- Babu Sam, D., Agarwalla, A., Joseph, J., Sindagi, V. A., Babu, R. V., and Patel, V. M. Completely self-supervised crowd counting via distribution matching. In *European Conference on Computer Vision*, pp. 186–204. Springer, 2022.
- DJukic, N., Luke, A., Zavrtanik, V., and Kristan, M. A low-shot object counting network with iterative prototype adaptation. In *Proceedings of the IEEE/CVF International Conference on Computer Vision*, pp. 18872–18881, 2023.
- D’Alessandro, A., Mahdavi-Amiri, A., and Hamarneh, G. Afreeca: Annotation-free counting for all. In *European Conference on Computer Vision*, pp. 75–91. Springer, 2024.
- Girshick, R. Fast r-cnn. In *Proceedings of the IEEE international conference on computer vision*, pp. 1440–1448, 2015.
- He, J., Liu, B., Cao, F., Xu, J., and Xiao, Y. Few-shot object counting with dynamic similarity-aware in latent space. *IEEE Transactions on Geoscience and Remote Sensing*, 62:1–14, 2024.
- Hobley, M. and Prisacariu, V. Learning to count anything: Reference-less class-agnostic counting with weak supervision. *Proceedings of the IEEE/CVF Conference on Computer Vision and Pattern Recognition*, 2023.
- Hsieh, M.-R., Lin, Y.-L., and Hsu, W. H. Drone-based object counting by spatially regularized regional proposal network. In *Proceedings of the IEEE international conference on computer vision*, pp. 4145–4153, 2017.
- Huang, Y., Ranjan, V., and Hoai, M. Interactive class-agnostic object counting. In *Proceedings of the IEEE/CVF International Conference on Computer Vision*, pp. 22312–22322, 2023.
- Huang, Z., Dai, M., Zhang, Y., Zhang, J., and Shan, H. Point segment and count: A generalized framework for object counting. In *Proceedings of the IEEE/CVF Conference on Computer Vision and Pattern Recognition*, pp. 17067–17076, 2024.
- Hui, X., Wu, Q., Rahmani, H., and Liu, J. Class-agnostic object counting with text-to-image diffusion model. In *European Conference on Computer Vision*, pp. 1–18. Springer, 2024.
- Jiang, R., Liu, L., and Chen, C. Clip-count: Towards text-guided zero-shot object counting. In *Proceedings of the 31st ACM International Conference on Multimedia*, pp. 4535–4545, 2023.
- Kang, S., Moon, W., Kim, E., and Heo, J.-P. Vlcounter: Text-aware visual representation for zero-shot object counting. In *Proceedings of the AAAI Conference on Artificial Intelligence*, volume 38, pp. 2714–2722, 2024.
- Kirillov, A., Mintun, E., Ravi, N., Mao, H., Rolland, C., Gustafson, L., Xiao, T., Whitehead, S., Berg, A. C., Lo, W.-Y., et al. Segment anything. In *Proceedings of the IEEE/CVF international conference on computer vision*, pp. 4015–4026, 2023.
- Langley, P. Crafting papers on machine learning. In Langley, P. (ed.), *Proceedings of the 17th International Conference on Machine Learning (ICML 2000)*, pp. 1207–1216. Stanford, CA, 2000. Morgan Kaufmann.
- Lempitsky, V. and Zisserman, A. Learning to count objects in images. *Advances in neural information processing systems*, 23, 2010.
- Li, S., Chang, F., and Liu, C. Bi-directional dense traffic counting based on spatio-temporal counting feature and counting-lstm network. *IEEE Transactions on Intelligent Transportation Systems*, 22(12):7395–7407, 2020.
- Lin, Y., Xu, H., Liu, L., and Shi, J. Q. A simple-but-effective baseline for training-free class-agnostic counting. In *2025 IEEE/CVF Winter Conference on Applications of Computer Vision (WACV)*, pp. 8155–8164. IEEE, 2025.
- Liu, C., Zhong, Y., Zisserman, A., and Xie, W. Countr: Transformer-based generalised visual counting. *arXiv preprint arXiv:2208.13721*, 2022.
- Liu, J., Gao, C., Meng, D., and Hauptmann, A. G. Decidenet: Counting varying density crowds through attention guided detection and density estimation. In *Proceedings of the IEEE conference on computer vision and pattern recognition*, pp. 5197–5206, 2018.
- Liu, S., Zeng, Z., Ren, T., Li, F., Zhang, H., Yang, J., Jiang, Q., Li, C., Yang, J., Su, H., et al. Grounding dino: Marrying dino with grounded pre-training for open-set object detection. In *European conference on computer vision*, pp. 38–55. Springer, 2024.

- Lu, E., Xie, W., and Zisserman, A. Class-agnostic counting. In *Asian conference on computer vision*, pp. 669–684. Springer, 2018.
- Ma, Z., Hong, X., and Shangguan, Q. Can sam count anything? an empirical study on sam counting. *arXiv preprint arXiv:2304.10817*, 2023.
- Mondal, A., Nag, S., Zhu, X., and Dutta, A. Omnicount: Multi-label object counting with semantic-geometric priors. In *Proceedings of the AAAI Conference on Artificial Intelligence*, volume 39, pp. 19537–19545, 2025.
- Pacini, G., Bianchi, L., Ciampi, L., Messina, N., Amato, G., and Falchi, F. Countingdino: A training-free pipeline for class-agnostic counting using unsupervised backbones. *arXiv preprint arXiv:2504.16570*, 2026.
- Paul Cohen, J., Boucher, G., Glastonbury, C. A., Lo, H. Z., and Bengio, Y. Count-ception: Counting by fully convolutional redundant counting. In *Proceedings of the IEEE International conference on computer vision workshops*, pp. 18–26, 2017.
- Pelhan, J., Lukezic, A., Zavrtanik, V., and Kristan, M. A novel unified architecture for low-shot counting by detection and segmentation. *Advances in Neural Information Processing Systems*, 37:66260–66282, 2024a.
- Pelhan, J., Zavrtanik, V., Kristan, M., et al. Dave-a detect-and-verify paradigm for low-shot counting. In *Proceedings of the IEEE/CVF Conference on Computer Vision and Pattern Recognition*, pp. 23293–23302, 2024b.
- Qian, Y., Guo, Z., Deng, B., Lei, C. T., Zhao, S., Lau, C. P., Hong, X., and Pound, M. P. T2icount: Enhancing cross-modal understanding for zero-shot counting. In *Proceedings of the Computer Vision and Pattern Recognition Conference*, pp. 25336–25345, 2025.
- Radford, A., Kim, J. W., Hallacy, C., Ramesh, A., Goh, G., Agarwal, S., Sastry, G., Askell, A., Mishkin, P., Clark, J., et al. Learning transferable visual models from natural language supervision. In *International conference on machine learning*, pp. 8748–8763. PmLR, 2021.
- Ranjan, V., Sharma, U., Nguyen, T., and Hoai, M. Learning to count everything. In *Proceedings of the IEEE/CVF Conference on Computer Vision and Pattern Recognition*, pp. 3394–3403, 2021.
- Shi, M., Lu, H., Feng, C., Liu, C., and Cao, Z. Represent, compare, and learn: A similarity-aware framework for class-agnostic counting. In *Proceedings of the IEEE/CVF Conference on Computer Vision and Pattern Recognition*, pp. 9529–9538, 2022.
- Shi, Z., Sun, Y., and Zhang, M. Training-free object counting with prompts. In *Proceedings of the IEEE/CVF Winter Conference on Applications of Computer Vision*, pp. 323–331, 2024.
- Siddiqui, M. I., Sheikh, M. U., Abid, H., and Khan, M. H. Persense: Training-free personalized instance segmentation in dense images. *BMVC*, 2025.
- Tyagi, A. K., Mohapatra, C., Das, P., Makharia, G., Mehra, L., AP, P., et al. Degpr: Deep guided posterior regularization for multi-class cell detection and counting. In *Proceedings of the IEEE/CVF Conference on Computer Vision and Pattern Recognition*, pp. 23913–23923, 2023.
- Wimmer, T., Truong, P., Rakotosaona, M.-J., Oechsle, M., Tombari, F., Schiele, B., and Lenssen, J. E. Anyup: Universal feature upsampling. *arXiv preprint arXiv:2510.12764*, 2025.
- Xu, J., Le, H., Nguyen, V., Ranjan, V., and Samarasinghe, D. Zero-shot object counting. In *Proceedings of the IEEE/CVF Conference on Computer Vision and Pattern Recognition*, pp. 15548–15557, 2023.
- Yang, S.-D., Su, H.-T., Hsu, W. H., and Chen, W.-C. Class-agnostic few-shot object counting. In *Proceedings of the IEEE/CVF Winter Conference on Applications of Computer Vision*, pp. 870–878, 2021.
- Zhai, W., Xing, X., Gao, M., and Li, Q. Zero-shot object counting with vision-language prior guidance network. *IEEE Transactions on Circuits and Systems for Video Technology*, 2024.
- Zhang, S., Zhou, Q., and Ke, W. Enhancing zero-shot object counting via text-guided local ranking and number-evoked global attention. In *Proceedings of the IEEE/CVF International Conference on Computer Vision*, pp. 21097–21106, 2025.
- Zhu, H., Yuan, J., Yang, Z., Guo, Y., Wang, Z., Zhong, X., and He, S. Zero-shot object counting with good exemplars. In *European Conference on Computer Vision*, pp. 368–385. Springer, 2024.

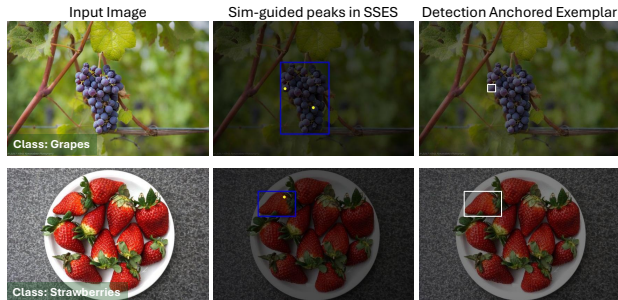


Figure 8. Visualization of SSES peak detection under multi-instance and single-instance coarse boxes. (Top row) When the initial detector box contains multiple objects, SSES identifies multiple high-similarity peaks within the coarse region, each serving as a point prompt to SAM and enabling refinement into a clean single-instance exemplar. (Bottom row) When the coarse region already corresponds to a confident single-instance detection, peak detection consistently falls on the same object, yielding a mask identical to the detector’s output. In this case, SSES functions as a verification step, retaining the original GroundingDINO box as a reliable exemplar.

A. Appendix

A.1. Ablation on k peaks in SSES module

Similarity-guided SAM-based Exemplar Selection (SSES) in Detection-Anchored Exemplar (DAE) stage, refines the initial-box selection into a clean, single-instance exemplar by jointly leveraging text-conditioned similarity map and SAM’s segmentation. It first locates the most text-aligned subregions within the coarse box by detecting high-confidence peaks in the similarity map using an adaptive percentile-relaxation strategy, ensuring robust peak detection under both strong and weak similarity patterns. As illustrated in Fig. 8 and 9, each detected peak serves as a point prompt to SAM, producing a set of candidate masks that are then evaluated using a composite score combining semantic alignment (mean percentile rank of similarities within the mask) and spatial purity (normalized entropy). This scoring mechanism prioritizes masks that are simultaneously text-consistent and instance-coherent, allowing SSES to reliably isolate single-object exemplars even in cluttered or ambiguous detections. We empirically set the maximum number of peaks at $k = 16$, which provides the best trade-off between coverage and precision for counting performance, with an ablation over $k = 4, 8, 16$ reported in Table 6.

A.2. P2P Prompting and Single-Instance Filtering

We present additional qualitative analysis illustrating the P2P prompting process and the impact of single-instance filtering. As shown in Fig. 10, given the exemplar from the DAE stage, a density map is first computed using the pretrained counter conditioned on this exemplar. Peaks de-

Table 6. Ablation on the maximum number of similarity peaks k used in SSES during the DAE stage. $k = 16$ provides the best balance of coverage and precision, yielding the lowest MAE and RMSE for our CountZES on the FSC-147 dataset.

Method	MAE	RMSE
CountZES ($k = 4$)	16.41	91.47
CountZES ($k = 8$)	16.22	91.65
CountZES ($k = 16$)	15.77	91.40

tected within the density map serve as point prompts to SAM, which generates corresponding masks and bounding boxes. These boxes are then filtered using RoI-count to retain only single-instance exemplars. As observed, this filtering refines the pool of candidate exemplars by discarding multi-instance or noisy regions. The resulting single-instance boxes are subsequently passed to the Pseudo-GT Guided Exemplar Selection (GGES) module to identify the final exemplar in the DGE stage.

A.3. Mathematical Details

Entropy Computation. For each candidate detection box $\mathbf{b}_i = (x_0, y_0, x_1, y_1)$, we extract the CLIP similarity values from the similarity map $S \in [0, 1]^{H \times W}$ within the box region, forming a set $\mathcal{V}_i = \{S(x, y) \mid (x, y) \in \mathbf{b}_i\}$. To estimate the distribution of similarity responses, we construct a histogram with $B = 20$ equally spaced bins over the range $[0, 1]$, yielding an empirical probability mass function $h_i(k)$ for $k = 1, \dots, B$.

We compute the Shannon entropy of this distribution as

$$H(\mathbf{b}_i) = - \sum_{k=1}^B \tilde{h}_i(k) \log \tilde{h}_i(k), \quad (8)$$

where $\tilde{h}_i(k) = \frac{h_i(k) + \epsilon}{\sum_{j=1}^B (h_i(j) + \epsilon)}$ applies Laplace smoothing with $\epsilon = 10^{-8}$ for numerical stability. Intuitively, low entropy corresponds to spatially consistent and semantically coherent regions, while high entropy indicates mixed or noisy content. To enable fair comparison across candidate boxes, we further perform min-max normalization over all entropy values:

$$\hat{H}(\mathbf{b}_i) = \frac{H(\mathbf{b}_i) - H_{\min}}{H_{\max} - H_{\min} + \epsilon}, \quad (9)$$

where H_{\min} and H_{\max} denote the minimum and maximum entropy among valid detections, respectively.

Pseudo-GT Count Estimation. Let $\mathcal{B}_{\text{single}} = \{\mathbf{b}_i\}_{i=1}^N$ denote the set of candidate single-instance boxes obtained after single instance filtering via density-based ROI count. For each candidate box \mathbf{b}_i , we obtain a local count estimate by leveraging the pretrained off-the-shelf density estimator $f_{\text{cnt}}(\cdot)$:

$$\hat{c}_i = f_{\text{cnt}}(I, \mathbf{b}_i), \quad i = 1, \dots, N, \quad (10)$$

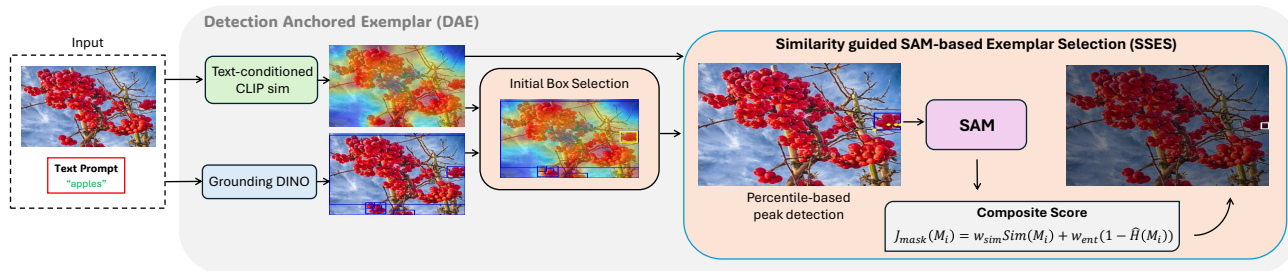


Figure 9. Illustration of the SSES module within the DAE stage. Given the detector-derived coarse box (in yellow), SSES leverages the text-conditioned CLIP similarity map to identify high-confidence response peaks using an adaptive percentile-based relaxation strategy. These peaks are used as point prompts to SAM, generating multiple candidate masks. Each mask is evaluated using a composite score that balances semantic alignment and spatial purity, and the highest-scoring mask is selected as the refined single-instance exemplar. The visual pipeline highlights how similarity-driven peak sampling and mask scoring together transform a noisy coarse region into a precise exemplar.

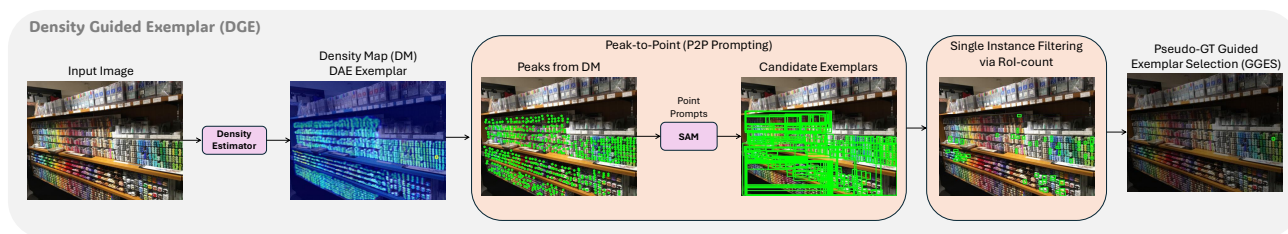


Figure 10. Overview of P2P prompting and single-instance filtering. Density peaks extracted from the density map serve as point prompts to SAM, whose masks are filtered via RoI-count to retain only single-instance regions before being passed to the GGES module for final selection in DGE stage.

where $\hat{c}_i \in \mathbb{Z}$ represents the predicted number of instances within \mathbf{b}_i . These per-box predictions are noisy due to imperfect localization and counter uncertainty.

To robustly aggregate these estimates, we model their empirical distribution using kernel density estimation (KDE), yielding a continuous probability density function:

$$\hat{p}(c) = \frac{1}{Nh} \sum_{i=1}^N K\left(\frac{c - \hat{c}_i}{h}\right), \quad (11)$$

where $K(\cdot)$ is a Gaussian kernel and h denotes the bandwidth parameter. The pseudo ground-truth count is then defined as the mode of this distribution:

$$c_{\text{pseudo}} = \arg \max_c \hat{p}(c). \quad (12)$$

In cases where the distribution exhibits negligible variance or insufficient distinct values, we adopt a robust fallback by assigning c_{pseudo} to the common value if all \hat{c}_i are identical, or to the rounded mean $\lfloor \frac{1}{N} \sum_{i=1}^N \hat{c}_i \rfloor$ otherwise. This aggregation strategy consolidates multiple uncertain predictions into a stable reference count while mitigating the influence of outliers.

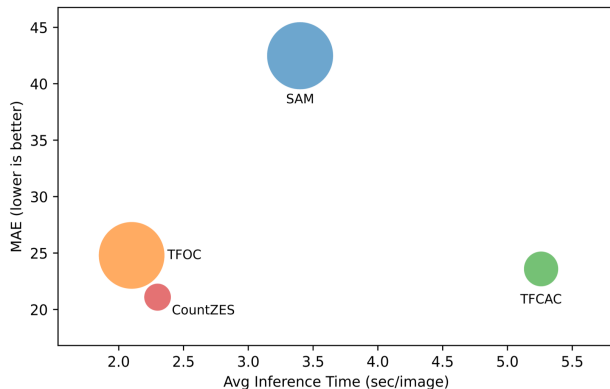


Figure 11. Performance–runtime tradeoff among inference-only zero-shot counting methods, where MAE is plotted against average inference time (sec/image) and bubble size represents RMSE. CountZES achieves the best accuracy with competitive inference efficiency.

A.4. Datasets

FSC-147 dataset (Shi et al., 2022) contains 6,135 paired images across 147 object classes and is specifically designed for class-agnostic counting. It is split into 3,659 training, 1,286 validation, and 1,190 test images with non-overlapping classes across splits, making it well-suited for evaluating zero-shot object counting. CARPK (Hsieh

et al., 2017) dataset provides a bird’s-eye view of 89,777 cars across 1,448 parking-lot images, serving as a standard benchmark for assessing cross-domain generalization from natural to aerial scenes. The recently introduced PerSense-D dataset (Siddiqui et al., 2025) serves as a dense counting benchmark, comprising 717 images spanning 28 object categories, with an average of 53 target instances per image and a total of 36,837 annotated objects across the dataset. VGG dataset (Lempitsky & Zisserman, 2010) includes 200 fluorescence-light microscopy images containing simulated bacterial cells, each image featuring approximately 174 ± 64 overlapping cells at varying focal depths to emulate realistic microscopic imaging conditions. Finally, MBM (modified bone marrow) dataset (Paul Cohen et al., 2017) contains 44 microscopic images with 126 ± 33 nuclei per image, representing challenging biological counting scenarios with high appearance variability.

A.5. Additional Qualitative Results

Fig. 12 presents additional qualitative results of CountZES on the FSC-147 dataset, showcasing its exemplar selection and counting performance across varied object densities and appearances.

A.6. Runtime Efficiency

We analyze the runtime efficiency of CountZES on FSC147 dataset, with all experiments conducted on a machine equipped with an NVIDIA RTX A5000 GPU. Figure. 11 illustrates the tradeoff between inference efficiency and counting accuracy among inference-only zero-shot counting methods, where MAE is plotted against average inference time and bubble size denotes RMSE. SAM exhibits high error despite moderate runtime (3.4 sec/image), while methods such as TFCAC incur substantial computational overhead (5.26 sec/image) without achieving corresponding accuracy improvements. TFOC achieves faster inference (2.1 sec/image) but suffers from noticeably higher error. In contrast, CountZES occupies the optimal region of the tradeoff space, achieving the lowest MAE and RMSE with competitive inference time (2.3 sec/image). These results demonstrate that the proposed multi-stage exemplar selection pipeline yields substantial performance gains without incurring very high computational cost, effectively balancing accuracy and efficiency in an inference-only setting.

A.7. Limitations

While CountZES demonstrates better generalization across domains, certain limitations stem from the use of off-the-shelf pre-trained components like density estimators and SAM. In cross-domain settings, where the pretrained counter is trained on distributions different from the target domain, this can lead to noise in peak detection via P2P

prompting. Also, as vanilla SAM lacks semantic awareness, a point prompt may yield only partial masks, capturing fragments of the object rather than complete instances. Although the scoring-based selection mechanism generally favors the most reliable exemplar at each stage, residual noise can still propagate when the majority of candidate exemplars are imperfect. As illustrated in Fig. 13 for the class “watches,” a point placed on the watch frequently segments only the dial while excluding the wristband, resulting in incomplete exemplar boxes. Additional examples in Fig. 14 highlight similar failures: for “nail polishes,” the mask captures only part of the bottle; for “comic books,” the prompt segments characters on the cover instead of the whole book; for “eggs,” SAM isolates only the yolk region; and for “sauce bottles,” it focuses on the label instead of the full object. Although the scoring mechanism generally prefers the best available candidates, residual noise can still propagate when most exemplars are imperfect. Nonetheless, a key strength of CountZES lies in its modular architecture. Each component, counter or segmentation backbone, can be seamlessly replaced with more advanced alternatives without altering the overall pipeline. This flexibility opens promising avenues for further enhancing cross-domain robustness and improving exemplar fidelity in future extensions.

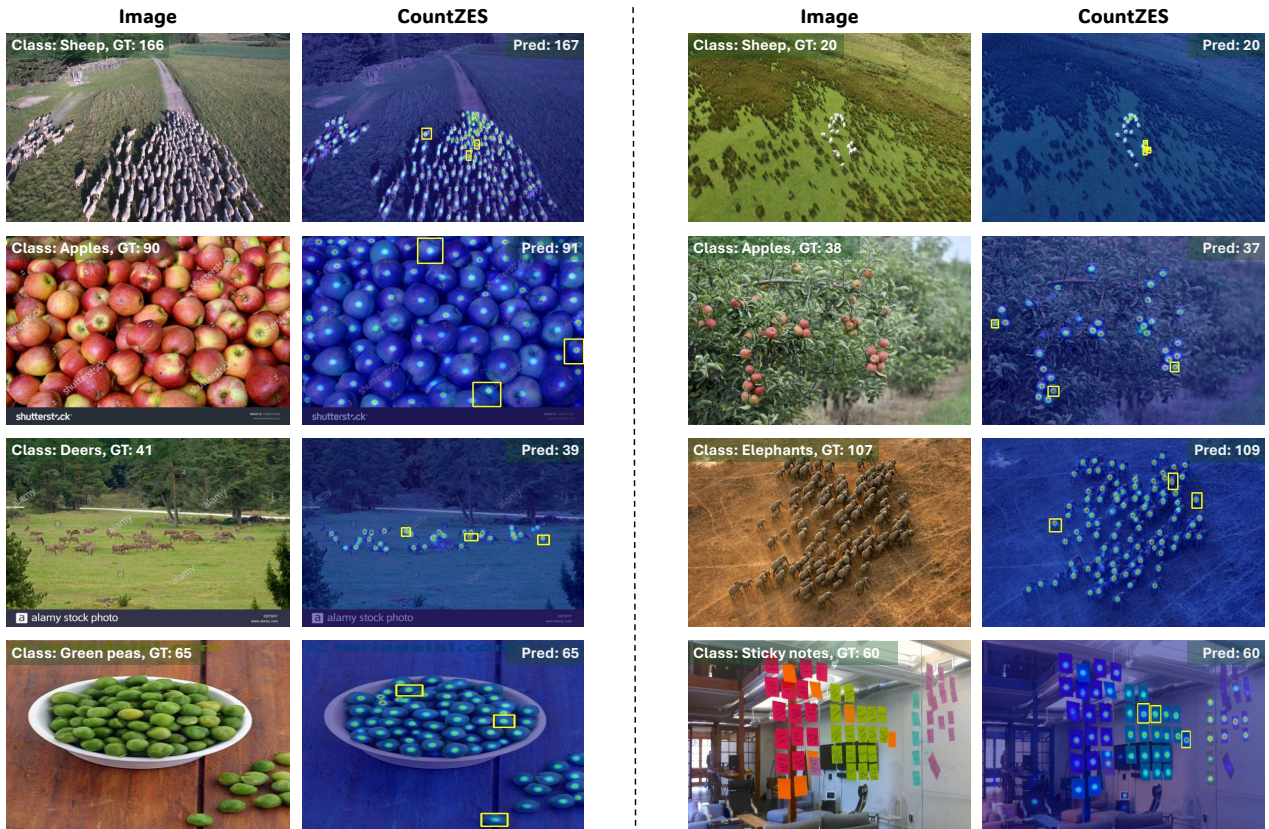


Figure 12. Additional qualitative results of CountZES on FSC-147 dataset.



Figure 13. Failure case illustrating CountZES selection of incomplete exemplar boxes for the class “watches.” Due to SAM’s limited semantic awareness, point prompts from density peaks segment only the watch dial, excluding the wristband, which produces partial masks and incomplete boxes that lead to suboptimal exemplar selection.



Figure 14. Additional failure cases highlighting CountZES selection of incomplete boxes as exemplars. For “nail polishes,” SAM-based point prompt segmentation in CountZES captures only partial objects; for “comic books,” point prompts isolate characters or cover details instead of the full book; for “eggs,” SAM segments only the yolk region; and for “sauce bottles,” it segments only the label instead of the whole bottle. These examples show how imperfect masks can impair downstream exemplar selection in CountZES.